C. R. Mecanique 343 (2015) 545–558

Contents lists available at ScienceDirect

Comptes Rendus Mecanique

www.sciencedirect.com

Discrete simulation of fluid dynamics

The permeability and quality of velocity field in a square array of solid and permeable cylindrical obstacles with the TRT–LBM and FEM Brinkman schemes

Goncalo Silva *, Irina Ginzburg

IRSTEA, Antony Regional Centre, HBAN, 1, rue Pierre-Gilles-de-Gennes, CS 10030, 92761 Antony cedex, France

ARTICLE INFO

Article history:
Received 12 December 2014
Accepted 5 May 2015
Available online 20 August 2015

Keywords:
Brinkman equation
Bimodal porous flow system
Lattice Boltzmann equation
TRT Brinkman model
Finite element Galerkin method

ABSTRACT

Using as a benchmark the porous flow in a square array of solid or permeable cylindrical obstacles, we evaluate the numerical performance of the two-relaxation-time lattice Boltzmann method (TRT–LBM) and the linear finite element method (FEM). We analyze the bulk, boundary and interface properties of the Brinkman-based schemes in staircase discretization on the voxel-type grids typical of porous media simulations. The effect of flow regime, grid resolution, and TRT collision degree of freedom Λ is assessed. In coarse meshes, the TRT may outperform the FEM by properly selecting Λ. Further, FEM is more oscillatory, a defect virtually suppressed in TRT with an improved strategy IBF and implicit accommodation of interface/boundary layers.

1. Introduction

Typically, a porous medium consists of a particulate system, possibly including pores or void spaces. Such a kind of structure can be found in a vast number of geological and industrial problems, e.g., hydrocarbon recovery or CO_2 sequestration, ground water flows, metal foams, fuel cells, and other kinds of engineering applications. Understanding transport phenomena in porous media is therefore vital, not only from the fundamental viewpoint, but also considering the development of many technological fields [1].

Usually, fluid flows in porous media cover three scales: the pore scale, the representative elementary volume (REV) scale, and the domain scale [2]. The REV is much larger than the pore scale, but much smaller than the domain scale. Here, details of the complex porous structure are averaged and accounted for in the form of a model permeability. In this context, the Brinkman equation [3] comes out as a much useful accommodation model, capable of describing the fluid dynamics from very impermeable porous flow, governed by Darcy's law, to open flow, governed by the Stokes equation. Owing to this versatility, the Brinkman equation provides a very attractive approach to study porous media flows. This fact manifests itself in the number of theoretical and numerical studies adopting Brinkman's equation, e.g., [4] and references therein.

The use of Brinkman's approach has been also applied since early times in the lattice Boltzmann method (LBM) [5]. Here, two modeling perspectives have gained popularity. In the first group, e.g., [6–10], the porous medium effect is explicitly accounted for as a forcing term introduced into the standard LBM. We denominate this group as Brinkman-force (BF) modeling approach [11,12]. In the second group, e.g., [13–17], the typical stream-and-collide rule of the LBM algorithm is modified with the introduction of a "partial-bounce-back" mechanism. This group is commonly denominated as gray lattice

* Corresponding author.
E-mail addresses: goncalo.silva@irstea.fr (G. Silva), irina.ginzburg@irstea.fr (I. Ginzburg).

http://dx.doi.org/10.1016/j.crme.2015.05.003
1631-0721/

Boltzmann (GLB) [11,15]. It turns out that differences between these two groups are more apparent than fundamental [11]. There exists an intrinsic link between the two ways of implementing Brinkman's model in LBM, meaning that one approach can be reduced to another [11,12].

Regardless of the approach implemented, the Brinkman LBM must satisfy an important requisite: *the modeled Brinkman equation must be linear with respect to fluid viscosity*. However, since the resistance (drag force) added to the flow equations varies with fluid velocity, the prescribed viscosity becomes modified via the discrete Laplacian applied to the Brinkman force [18]. This artefact inevitably introduces a non-linear dependency on the coefficient of the viscosity when a single collision rate is employed, e.g., the BGK–LBM [19]. To avoid this inconsistency, an alternative consists in adopting the two-relaxation-time (TRT) scheme [20], which is followed in this work.

The Brinkman LBM has been applied to a number of practical problems. The simplest example refers to the single or stratified heterogeneous porous channel. Since this case has an analytical solution, it has been explored rather extensively to evaluate the performance of the Brinkman LBM, e.g., [8–10,12], with the BF model and [13,15–17] with the GLB approach. Also, the famous benchmark test of lid-driven cavity flow has been studied for a cavity filled with a porous medium. However, owing to the lack of analytical solutions, Brinkman LBM results were compared to Finite Difference reference solutions [8,10]. Possibly the most challenging problem, in regular Cartesian geometries, is the modeling of porous flow in random media, e.g., [12]. Yet, once again, due to the lack of analytical solutions, the corresponding Brinkman LBM solutions have to be benchmarked against Finite Element Method (FEM) and corresponding Darcy's reference solutions.

In complement to these academic configurations, Brinkman LBM studies have been also applied to more realistic geometries, e.g., X-ray CT images of real porous media [17]. Here, the tortuosity of the flow system is typically resolved on a voxel-type grid, meaning that boundary and interface shapes get described in a staircase manner. Overall, this raises the question of the abilities and/or limitations of the numerical solutions to cope with such complex porous medium structures. To shed light over this issue, it would be convenient to have validation from a non-trivial benchmark test, where the geometry degree of complexity could represent the realistic porous configuration. A suitable candidate for this purpose is the study of a periodic array of permeable cylinders, so far restricted to specific configurations, e.g., [6,16]. Recently, this problem has been analytically approached for the most general configuration [21], *bimodal porous system*, at both low and high concentration of obstacles. The work [21] provides reference solutions to this problem class, applicable over an extended range of bimodal permeabilities and volume fractions.

In parallel, the theoretical and numerical analysis of the Brinkman LBM and FEM schemes was recently developed in [12], focusing on two main points. First, the discrete structure of those schemes with respect to bulk, boundary and interface conditions was analyzed. Second, an improved strategy, called IBF, which upgraded the traditional BF operation principle, was introduced. The present work can be considered as a numerical complement to study [12], whereby the one-dimensional flow analysis developed for channels is extended over a more complex geometrical configuration. With this work, we intend to address the following questions: (1) What is the effect of the flow dynamical regime, i.e. Stokes, Brinkman or Darcy, over the performance of the numerical scheme? (2) Do the improved characteristics of the IBF hold in a more complex flow geometry? (3) Up to which degree the (i) bulk error [18] and the lower-order accuracy of (ii) boundary and (iii) interface schemes, such as the bounce-back [22,23] and implicit interface conditions [20], play a role? (4) How does the additional TRT collision degree of freedom Λ operate over the aforementioned three effects? We will answer these questions by studying four distinguished structures in terms of their model parameters and discretization properties. For that, we will take as measures the accuracy of the estimated permeability and the quality of the velocity field.

This work is structured as follows. In Section 2 we describe the problem here used as a benchmark. In Section 3 we review the Brinkman numerical schemes employed, giving particular focus on the bulk, boundary and interface properties of the BF and IBF schemes. In Sections 4 and 5, we present our numerical results, discussing the points previously raised. Finally, Section 6 concludes the work.

2. Problem formulation

Consider the steady and incompressible viscous motion of a Newtonian fluid in a porous medium environment featuring a square array of porous cylindrical inclusions with different properties. The geometrical configuration is illustrated in Fig. 1(a). The fluid motion is assumed to develop in the creeping flow regime, where inertial effects are negligible. The most general description of this *two-dimensional* problem is given by Stokes–Brinkman–Darcy equations:

$$\vec{\nabla}\cdot\vec{u}^{(i)}=0,\qquad \vec{\nabla}p^{(i)}=\mu_{\mathrm{B}}\nabla^2\vec{u}^{(i)}-\frac{\mu}{k_i}\vec{u}^{(i)} \tag{1}$$

where the indices $i=1,2$ refer, respectively, to the domains inside and outside the inclusions, Fig. 1(a). Equations (1) solve for velocity vector $\vec{u}$ and pressure p; it contains as parameters Brinkman viscosity μ_{B}, fluid viscosity μ and permeability k. Based on the system periodicity, the problem can be reduced to the study of the unitary cell, as depicted in Fig. 1(b). In this work, two structures of inclusions are considered: (i) impermeable ($k_1=0$), and (ii) permeable ($k_1>0$).

(i) The first case adopts the typical no-slip boundary condition on the impermeable cylinder surface:

$$\vec{u}^{(2)}=\vec{0},\qquad \text{at}\quad r=R \tag{2}$$

This case is studied for two matrix flow conditions: (1) open ($k_2 = \infty$), Section 4.1, and (2) porous ($0 < k_2 < \infty$), Section 4.2.

(2) The second case adopts the continuity condition across the permeable cylinder interface:

$$\vec{u}^{(1)} = \vec{u}^{(2)}, \quad \vec{n} \cdot \bar{\bar{T}}^{(1)} = \vec{n} \cdot \bar{\bar{T}}^{(2)}, \qquad \text{at} \quad r = R \tag{3}$$

where $\mathbf{n}$ is the outward unit normal from the cylinder surface and $\bar{\bar{T}} = -p\bar{\bar{I}} + \mu_B \left(\vec{\nabla}\vec{u} + (\vec{\nabla}\vec{u})^T\right)$ is the stress tensor (which contains pressure and viscous stresses). This case is examined for two permeability configurations: (1) the matrix is more permeable than the inclusion ($k_2 > k_1$), Section 5.1, and (2) the matrix is less permeable than the inclusion ($k_2 < k_1$), Section 5.2. The first case considers inclusions as the most compact material, while the second configuration conceives inclusions as open fractures. For the purpose of the present study, the permeability range of inclusion and matrix regions are assumed to be $k_1 > 0$ and $k_2 > 0$, respectively. Their zero limits, towards a very impermeable Darcy regime, have been studied in [21], with focus on the link between the interface condition (Eq. (3)) and the discontinuous Beavers–Joseph interface condition [1,4].

While this problem is not accessible to exact solutions for the local velocity and pressure fields, analytical approximations exist, which allow us to estimate the global permeability of the system. In fact, the first problem of the Stokes flow around solid cylinders has been tackled in this way in a number of works, e.g., [24–27]. The Brinkman solution was recently extended in [21], employing two complementary theoretical approaches: the *cell model* [25,26], operated in the low volume fraction of inclusions, and the *lubrication theory* [27,28], applied in the opposite limit of high volume fraction. Hereafter, the accuracy of numerical schemes is evaluated on the basis of the permeability error:

$$\mathrm{err}(k) = \frac{k_{\mathrm{num}}}{k_{\mathrm{th}}} - 1, \qquad k_{\mathrm{num}} = \frac{\mu < \vec{u} >}{< -\vec{\nabla} p >} \tag{4}$$

The reference theoretical value k_{th} is found in [21,24], and k_{num} is computed from $< \vec{u} >$, which is the numerical solution for the mean velocity in a periodic cell driven by the mean pressure gradient $< \vec{\nabla} p >$.

3. Numerical schemes overview

The numerical modeling of the problem described in Section 2 employs the TRT–LBM and the FEM. The focus of this study is put on the TRT–LBM, while the FEM is mainly used for comparison purposes. Below we summarize the main features of the two numerical schemes in terms of their bulk, boundary and interface modeling, further indicating their most relevant implementation aspects. A more detailed exposition of these topics can be found in [12].

3.1. TRT–LBM: bulk, boundary and interface

We consider the D2Q9 discrete velocity model [19], which features one immobile $\vec{c}_0 = \vec{0}$ and $Q_m = Q - 1$ non-zero velocity vectors $\vec{c}_q$ per grid node. The LBM solves for the populations $f_q(\vec{r}, t)$ moving on grid nodes along a succession of streaming and collision steps. The streaming step performs a simple shift of populations to the neighboring nodes. The collision step takes place locally, relaxing populations towards a prescribed equilibrium state $e_q(\vec{r}, t)$. We operate the collision with the TRT model [20], which is constructed on the symmetry argument $\vec{c}_q = -\vec{c}_{\bar{q}}$. On this basis, populations are decomposed into symmetric $f_q^+ = \frac{1}{2}\left(f_q + f_{\bar{q}}\right)$ and anti-symmetric $f_q^- = \frac{1}{2}\left(f_q - f_{\bar{q}}\right)$ components, with immobile population $f_0^+ = f_0$. The relaxation process is therefore controlled by two collision eigenvalues: $\{s^+, s^-\} \in]0, 2[$, for symmetric and anti-symmetric modes, respectively. They define two eigenvalue functions $\Lambda^{\pm} = \left(\frac{1}{s^{\pm}} - \frac{1}{2}\right)$, whose product $\Lambda = \Lambda^+\Lambda^-$ controls non-dimensional steady-state solutions [18].

The update rule of the TRT–LBM, for streaming and collision steps, reads:

$$f_q(\vec{r} + \vec{c}_q, t+1) = \tilde{f}_q(\vec{r}, t), \quad q = 0, 1, \ldots, Q-1 \tag{5a}$$

$$\tilde{f}_q(\vec{r}, t) = [f_q + g_q^+ + g_q^-](\vec{r}, t), \quad q = 0, 1, \ldots, \tfrac{Q_m}{2}$$

$$\tilde{f}_{\bar{q}}(\vec{r}, t) = [f_{\bar{q}} + g_q^+ - g_q^-](\vec{r}, t), \quad q = 1, \ldots, \tfrac{Q_m}{2} \tag{5b}$$

where $\tilde{f}_q$ denotes the post-collision state of populations f_q, with $g_q^{\pm} = -s^{\pm}(f_q^{\pm} - e_q^{\pm})$. The Stokes–Brinkman (BF) model [12] prescribes the equilibrium $e_q^{\pm}$ as follows:

$$e_q^+(\vec{r}, t) = t_q^* c_s^2 \rho = t_q^* P(\rho), \quad e_0^+(\vec{r}, t) = \rho - 2\sum_{q=1}^{Q_m/2} e_q^+, \qquad e_q^-(\vec{r}, t) = t_q^*(\rho_0 \vec{u} \cdot \vec{c}_q) + \Lambda^- t_q^*(\vec{F} \cdot \vec{c}_q) \tag{6}$$

Table 1
Summary of effective parameters impacting the discretization of an horizontal porous channel flow: relative viscosity correction $\delta(B)$, Eq. (8); and coefficients $\alpha^{\pm}$ of boundary and interface velocity condition, respectively, Eq. (9) and Eq. (10b). The last column indicates the range of B that guarantees that ν remains positive. Rather than constants, B and Λ are locally prescribed parameters.

	δ	$\alpha^{+}/(1+\delta)$	$\alpha^{-}/(1+\delta)$	$\nu > 0$
BF	$\frac{8\Lambda-3}{12}B$	1	$\frac{16}{3}\Lambda$	if $\Lambda < \frac{3}{8} \Rightarrow B < \frac{12}{3-8\Lambda}$, else $\forall B$
IBF	0	$\frac{4(3+2\Lambda B)}{3(4+B)}$	$\frac{16}{3}\Lambda$	$\forall B$
FEM	$-\frac{B}{6}$	–	–	$B < 6$

where $c_s^2 \in]0,1]$ is a free parameter and t_q^* are isotropic hydrodynamic weights $\{t_q^{*(I)}, t_q^{*(II)}\} = \{\frac{1}{3}, \frac{1}{12}\}$ for D2Q9. The mass and momentum are recovered as $\rho = \sum_{q=0}^{Q-1} f_q$ and $\rho_0 \vec{u} = \sum_{q=1}^{Q-1} f_q \vec{c}_q + \frac{1}{2}\vec{F}$. Here, $\vec{F}$ is an externally imposed body force, assumed as $\vec{F} = \vec{F}^{(p)} + \vec{F}^{(r)}$, where: (i) $\vec{F}^{(p)}$ models the action of an uniform body force, such as the gravity or a driving pressure gradient, and (ii) $\vec{F}^{(r)}$ models the resistance introduced by the porous medium. In the TRT model, the Brinkman viscosity is given by $\mu_B = \rho_0 \nu_B = \frac{\rho_0 \Lambda^+}{3}$. The steady momentum balance established by Eqs. (5) and (6) read [12,18]:

$$\overline{\nabla} P - \vec{F}^{(p)} - \vec{F}^{(r)} = \nu_B(1+\delta^{is})\rho_0 \bar{\Delta}^2 \vec{u} - 2(\Lambda - \tfrac{1}{4}) \sum_{q=1}^{Q\,m/2} \bar{\Delta}_q^2 g_q^- \vec{c}_q \tag{7}$$

where $\bar{\Delta}^2$ denotes the discrete Laplacian operator and $\bar{\Delta}_q^2 g_q^-(\vec{c}_q(\vec{r}) = g_q^-(\vec{r}+\vec{c}_q) - 2g_q^-(\vec{r}) + g_q^-(\vec{r}-\vec{c}_q)$, with $\nu_B = \frac{\Lambda^+}{3}$, $\delta^{is} = -\frac{\Lambda}{3}B$ and $B = \frac{B_f}{\nu_B}$ with $B_f = \frac{\nu}{k}$. Note that δ^{is} is the isotropic viscosity correction due to the force variation while the last term in Eq. (7), i.e. $-2(\Lambda - \frac{1}{4})\sum_{q=1}^{Q\,m/2} \bar{\Delta}_q^2 g_q^- \vec{c}_q$, further modifies the effective viscosity by introducing an anisotropic correction [18]. To understand its effect, we recall that, in a force-driven horizontal channel-flow configuration (with $\overline{\nabla} P = 0$), the post-collision quantity reads $g_q^-(y) = 3t_q^* c_{qx} c_{qy}^2 F_x(y)$ (the proof of this result is given in [12,18]; the case when $\overline{\nabla} P \neq 0$ is also discussed in [12], both of which yielding identical conclusions). After substituting the Brinkman forcing into $g_q^-(y)$, the outcome will couple with the discrete Laplacian of $\vec{u}$ in Eq. (7), altering the effective viscosity coefficient by a quantity $\delta(B,\Lambda)$ defined as

$$\delta(B,\Lambda) = \delta^{is} + (\Lambda - \tfrac{1}{4})B = \frac{B(8\Lambda - 3)}{12} \tag{8}$$

When $\delta < -1$, the effective viscosity becomes negative, which causes numerical oscillations in the solutions. On the other hand, this cannot occur when $\Lambda \geq 3/8$, see the BF conditions summarized in Table 1.

The solid-wall condition is modeled with the *bounce-back* rule: $f_{\bar{q}}(\vec{r}_b, t+1) = \tilde{f}_q(\vec{r}_b, t)$, when $\vec{r}_b + \vec{c}_q$ is a solid node. This scheme prescribes the no-slip wall condition implicitly, as a second-order Taylor-type condition. For a straight channel of width H, the bounce-back steady-state closure relation reads [12]:

$$u_j \pm \tfrac{1}{2}\alpha^+ \bar{\Delta}_y u_j + \tfrac{1}{8}\alpha^- \bar{\Delta}_y^2 u_j|_{y_j = \pm H \mp \frac{1}{2}} = 0 \tag{9}$$

with coefficients $\alpha^{\pm}$ given in Table 1. This means that the no-slip condition can be satisfied only up to the truncation order of Eq. (9) in any flow. It follows that in Brinkman flow, even the first-order wall location is not, in general, a predetermined feature, as $\alpha^{\pm}$ depends on Λ, see Table 1; hereby, a reference value making it exact for open Poiseuille channel flow is $\Lambda = 3/16$ [22,23]. Actually, since we are modeling a cylindrical obstacle, the natural procedure should adopt an higher-order boundary technique, where the curved surface could be described explicitly. However, the present work is considered in the context of porous media flows, where, generally, the boundary is not a well-defined feature, thus making the bounce-back a reasonable candidate since it has some advantages, such as: (1) local implementation, (2) mass conservation, or (3) supporting the parameterization properties of the TRT scheme in the bulk [12,18].

The LBM interface condition employed in this work is of implicit type. That means it arises implicitly when populations carry their properties from one phase to another [20]. In stratified channels, the steady-state closure relation for the interface takes the form of the Taylor-type finite-difference approximations of the stress and velocity continuity conditions [11,12]:

$$\|\nu_i(\bar{\Delta}_y u_j^{(i)} \pm \tfrac{1}{2}\bar{\Delta}_y^2 u_j^{(i)})\|_{Y_i \mp \frac{1}{2}} = 0\,, \quad \nu_i = \nu_B^{(i)}(1+\delta_i) \tag{10a}$$

$$\|u_j^{(i)} \pm \tfrac{1}{2}\alpha_i^+ \bar{\Delta}_y u_j^{(i)} + \tfrac{1}{8}\alpha_i^- \bar{\Delta}_y^2 u_j^{(i)})\|_{Y_i \mp \frac{1}{2}} = 0 \tag{10b}$$

where the index i labels the layer and $\|\psi\|_{Y_i \mp \frac{1}{2}} = 0$ means $\psi_i(Y_i - \frac{1}{2}) = \psi_{i+1}(Y_i + \frac{1}{2})$. The finite difference operators apply to the velocity solution of the same layer, as explained in [11,12]. The coefficients $\alpha_i^{\pm}$ in the velocity-continuity condition and relative viscosity correction δ in the stress-continuity condition are given in Table 1. The continuity conditions

can be satisfied only up to the truncation order of the Taylor condition, and its formal accuracy is further affected by Λ-dependent coefficients. This may lead to jumps in the macroscopic solutions across the interface. To overcome this defect, explicit interface conditions could be developed instead. However, we opted to keep up with the implicit ones, following the justification adopted for the bounce-back. Since the precise description of interfaces is generally not available in porous media, the use of more complex techniques is not compensatory.

3.2. IBF scheme

In straight porous channel configurations, there are many possible ways to make the viscosity coefficient δ vanish; some of them can be found in [11,12]. Among such strategies, an interesting candidate is the IBF scheme [12]. The IBF applies over the standard TRT update rule, Eqs. (5), with equilibrium and forcing given by Eq. (6), but it modifies the eigenvalue of the symmetric component: $s^+ \to s^+_*$. Giving the locally prescribed input quantities: (i) $\Lambda^+ = 3\nu_B$, (ii) $B_f = \nu/k$, and (iii) Λ; the IBF operates with two local eigenvalue functions $\Lambda^\pm_*$ given as follows:

$$\Lambda^+_*(B,\nu_B,\Lambda) = \frac{1}{s^+_*} - \frac{1}{2} = \frac{9(4+B)\nu_B}{4(3+2B\Lambda)}, \quad \Lambda^-_* = \frac{1}{s^-_*} - \frac{1}{2} = \frac{\Lambda}{\Lambda^+}, \quad \Lambda^+ = 3\nu_B, \quad B = \frac{B_f}{\nu_B} = \frac{\nu}{\nu_B k} \tag{11}$$

The effective "magic" parameter of IBF is $\Lambda_*(B,\Lambda)$, which is independent of ν_B, which means that, for fixed Λ and $\frac{\nu}{\nu_B}$, it varies alone with the inverse of the permeability distribution:

$$\Lambda_*(B,\Lambda) = \Lambda^+_*\Lambda^-_* = \frac{\Lambda^+_*}{\Lambda^+}\Lambda = \frac{3(4+B)\Lambda}{4(3+2B\Lambda)}, \quad \lim_{B\to 0}\Lambda_* = \Lambda, \quad \lim_{B\to\infty}\Lambda_* = \frac{3}{8} \tag{12}$$

The BF and IBF differ for symmetric eigenvalue Λ^+_*, unless either $B = 0$ (Stokes flow) or $\Lambda = \frac{3}{8} = \Lambda_*$, $\forall B$ (any regime). By construction, the IBF has zero viscosity correction $\delta = 0$ in a straight channel (the solution for $\Lambda^+_*(B,\nu_B,\Lambda)$ in the diagonal channel case is straightforward to extend, see [12]). This improvement acts simultaneously over the bulk solution and the coefficients affecting boundary and interface conditions, see Table 1. Indeed, numerical tests performed in single and stratified porous channels confirm that the IBF makes the oscillations displayed by the BF in the bulk completely vanish (e.g., compare Fig. 7 to Fig. 14 in [12]), and it also enhances the solution behavior on the boundary and interface vicinity. This last feature is improved through the curvature coefficient α^-, which in the IBF becomes independent of the flow regime, i.e. its functional form becomes that typically found in Stokes' flow [22,23].

In summary, by suppressing oscillations and providing a better accommodation of velocity profiles with either multi-layered or random permeability distributions, the accuracy level of the IBF improves that of the BF. In this work, we are interested in verifying whether these superior characteristics hold for non-straight boundary/interface configurations.

3.3. FEM: general features in bulk, boundary and interface

For comparison purposes, the problem described in Section 2 is also solved with the Finite-Element Method (FEM). A more detailed account on the similarity and distinctness between the LBM and FEM, in dealing with bulk, boundary and interface, is discussed in [12]. Succinctly, the FEM formulation performs the following steps. The governing equations of the problem, Eqs. (1), are written in weighted integral form, with their derivatives decreasing the differential order, by using the Gauss–Green theorem, a process called the weak formulation [29]. Subsequently, the continuous solution is approximated by a trial solution, which is defined in a discrete space, here assumed an a uniform Cartesian grid. A linear shape is adopted for the trial functions that approximate the solution in between nodes. Finally, the family of weight functions is chosen such as to be equal to the trial functions; this approximation is called the Galerkin method [29]. The FEM implementation was operated with the commercial software COMSOL [30].

In terms of discretization, unlike the LBM where nodes are cell-centered, in the FEM they locate at the cell vertexes. Despite this difference, bulk channel solutions in LBM and FEM display a similar structure: in FEM, the effective viscosity coefficient is given by $\delta = -B/6$, which is a particular solution to TRT with $\Lambda = 1/8$, [12]. However, two different methodologies are adopted in the prescription of boundary and interface conditions. In FEM, the wall boundary conditions are enforced exactly at grid nodes, and the interface continuity conditions are also set at grid nodes, subject to typical bulk node rules. At the same time, the effective stress-continuity condition reads $\|\nu_i \bar{\Delta}_y u^{(i)}_j\|_{\gamma_i} = 0$, where $\nu_i = \nu^{(i)}_B(1+\delta_i)$. The enforcement of either interface-continuity or no-slip velocity conditions at grid nodes gives rise to strong oscillations, in agreement with the exact channel solutions to the FEM [12].

3.4. Implementation aspects

The periodic square array arrangement of inclusions is reduced to a unitary cell, subject to periodic boundary conditions, see Fig. 1(b). The flow is driven by an external body force $\vec{F}^p$, which mimics the effect of an applied constant pressure gradient in Eq. (4). Simulations are initialized for a rest state $\vec{u} = \vec{0}$ and an uniform pressure field $p = c_s^2\rho$ with $\rho = 1$ [in simulation units]. The steady state is assumed to be reached: (1) in LBM for the magnitude of the relative difference in

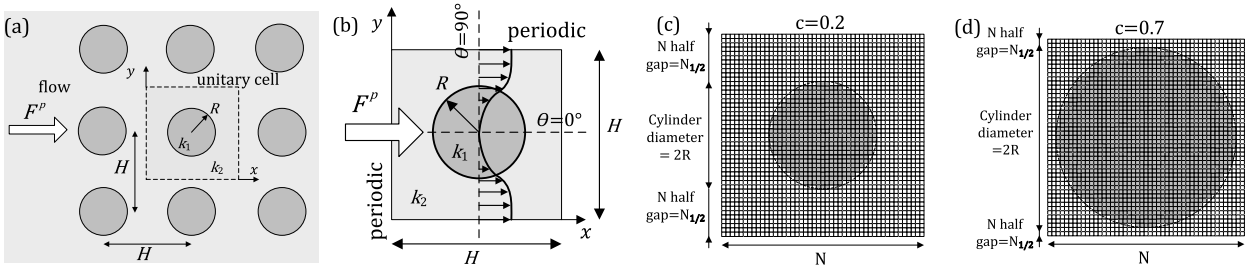

Fig. 1. (Color online.) Schematic representation of the problem studied. (a) Illustration of periodic square array of cylindrical obstacles. (b) Detail of unitary cell (featuring definitions of most relevant parameters adopted in this study). (c) and (d) Discrete representation of unitary cell for low/high volume fractions, $c = \pi R^2/H^2$, (c) $c = 0.2$ and (d) $c = 0.7$.

Table 2
Influence of geometrical discretization error (i.e. staircase description of the circle) on the effective volume fraction of the system, and respective impact on the predicted permeability of Stokes flow around square array of solid cylinders, [24], for two volume fractions $c = 0.2$ and $c = 0.7$, where N is the cell size, $N_{1/2}$ is the half-gap size (i.e. $N_{1/2} = N/2 - R$), c_{num} is the effective volume fraction for the discrete system, and the error measures are $err(c) = \frac{c_{\text{num}}}{c} - 1$ and $err(k_{\text{th}}) = \frac{k_{\text{th}}(c_{\text{num}})}{k_{\text{th}}(c)} - 1$.

N	$c = 0.2$				$c = 0.7$			
	$N_{1/2}$	c_{num}	$err(c)$ [%]	$err(k_{\text{th}})$ [%]	$N_{1/2}$	c_{num}	$err(c)$ [%]	$err(k_{\text{th}})$ [%]
33	8	0.1983	−0.85	1.11	1	0.6795	−2.9	74.34
55	14	0.2036	1.80	−2.31	2	0.6717	−4.04	109.69
99	25	0.2016	0.80	−1.03	3	0.6909	−1.30	29.83
133	33	0.1985	−0.75	0.98	4	0.6929	−1.01	22.86
155	38	0.1995	−0.25	0.32	4	0.7049	0.70	−14.10
199	49	0.1985	−0.75	0.98	5	0.7012	0.17	−3.58
251	62	0.2007	0.35	−0.45	7	0.6997	−0.04	0.91
501	124	0.2001	0.05	0.06	14	0.6999	−0.01	0.30
751	186	0.1999	−0.05	−0.06	21	0.6999	−0.01	0.30

permeability $|k(t)/k(t - t_a) - 1| < 10^{-10}$, with $t_a = 10^3$ simulation time steps; (2) in FEM COMSOL for the magnitude of the relative residual smaller than 10^{-10} in GMRES iterative solver.

In both numerical schemes, the cylindrical obstacle is discretized on a regular grid in a staircase fashion. By defining the cylinder volume fraction as $c = \pi R^2/H^2$, see Fig. 1(b), the discretization error in the cylinder creates a mismatch between the discrete value c_{num} and c. This error source is summarized in Table 2, together with its impact on the predicted Stokes permeability k_{th}. The volume exclusion error displays a non-monotonic behavior with grid resolution, yet it stabilizes around a relatively small value at finer grids. This trend is verified for the two volume fractions studied here: dilute, $c = 0.2$, Fig. 1(c), and concentrated, $c = 0.7$, Fig. 1(d).

We use a numerical integration scheme, the mid-point rule, to compute the mean velocity $< \vec{u} >$. Since this numerical integration scheme is of lower order than the exact numerical solution, e.g., in channels, it is expected that k_{num} is affected by integration errors [2].

4. Solid inclusion: bounce-back analysis

4.1. Open flow

The Stokes flow is the simplest problem among all cases studied in this work. Here, the LBM accuracy is essentially controlled by three features: (1) the geometrical discretization error in the staircase boundary description, (2) the boundary location error due to the bounce-back, and (3) the integration error in estimating k_{num}. Their relative importance depends on the grid refinement level, as illustrated in the behavior of $err(k)$ curves in Fig. 2, panels (a) and (b).

For coarse meshes, we recognize a large variability of solutions with Λ. In fact, owing to the fact that the boundary location is a Λ-dependent feature, different Λ values make the gap between the cylindrical obstacle vary; while at high Λ, the section for the flow to pass is enlarged, at low Λ, it is narrowed. This explains why, for a fixed grid resolution, the permeability errors, $err(k)$ in Fig. 2, change their sign, going from $err(k) < 0$ at low Λ to $err(k) > 0$ at high Λ. A similar study was reported in [23] for a Stokes flow around regular and random arrays of spherical solid obstacles. The effect of Λ in a similar flow configuration was also of interest in [31]. Historically, the shift of the bounce-back boundary location with Λ was first identified for channel flows [22]. Since in this configuration, this error source is only significant for high Λ, it became commonplace believing that the bounce-back is safe to use when Λ is small, e.g., [32]. However, in line with [23], the present study confirms that in modeling the flow through fluid gaps the use of small Λ is equally harmful, particularly in narrow ones.

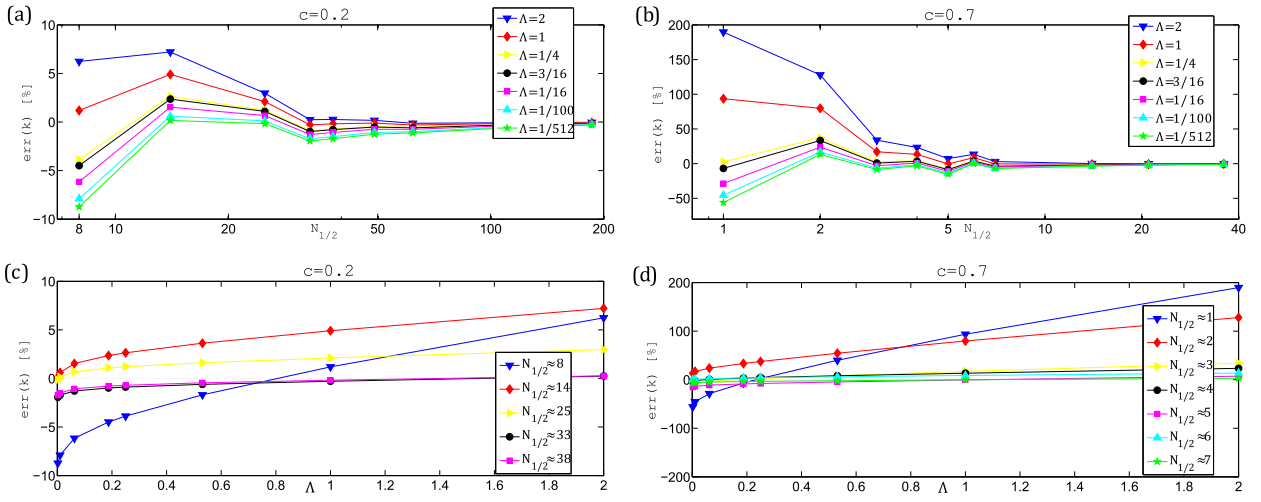

Fig. 2. (Color online.) Open flow around a solid cylinder. Panels (a) and (b): TRT error in permeability $err[k]$ as function of gap half-size $N_{1/2} = N/2 - R$, fixing Λ. Panels (c) and (d): TRT $err[k]$ as function of Λ, fixing $N_{1/2}$. Left $c = 0.2$ and right $c = 0.7$.

Table 3
Open flow around a solid cylinder. Interval of optimal Λ where $err(k) = 0$, range of analysis $\Lambda \in [\frac{1}{512}, 2]$. Results shown for 8 resolutions with the gap half-size $N_{1/2} = N/2 - R$, and low/high volume fractions c.

$c = 0.2$	$N_{1/2}$	8	14	25	33	38	49	62
	Λ	$[\frac{17}{32}, 1]$	$]0, \frac{1}{512}]$	$[\frac{1}{512}, \frac{1}{100}]$	$[1, 2]$	$[1, 2]$	$[1, 2]$	> 2
$c = 0.7$	$N_{1/2}$	1	2	3	4	5	6	7
	Λ	$[\frac{1}{4}, \frac{17}{32}]$	$]0, \frac{1}{512}]$	$[\frac{1}{16}, \frac{3}{16}]$	$[\frac{1}{100}, \frac{1}{16}]$	$[1, 2]$	$[\frac{1}{512}, \frac{1}{100}]$	$[1, 2]$

For fine meshes, all Λ solutions (virtually) collapse in a single curve. The vanishing of the relative importance of Λ is explained by this parameter scaling with the second-order terms in the bounce-back Taylor-type condition, see Eq. (9) with $\delta = 0$. Thereby, its impact reduces faster with resolution, making the permeability accuracy essentially controlled by the geometrical discretization error and the numerical integration error. Indeed, in the range of fine meshes where Λ solutions collapse, it can be confirmed that $err(k) \sim [-0.49, -0.03]$ [%] at $c = 0.2$ and $err(k) \sim [-2.24, -0.04]$ [%] at $c = 0.7$, which is in line with the order of magnitude of the geometrical discretization error, see $err(k_{\text{th}})$ in Table 2 (notice $err(k_{\text{th}})$ excludes integration error). Conversely, at coarser resolutions, we have $|err(k)| \gg |err(k_{\text{th}})|$, explained by the dominating effect of the bounce-back wall shifting error.

The panels (c) and (d) in Fig. 2 provide a different perspective to understand the aforementioned results. Explicitly, they show that, for a fixed grid resolution, increasing Λ, asymptotically, impacts the permeability error almost linearly. Still, the trend is not exactly linear, as demonstrated by $\frac{1}{2}[err(k[\Lambda_1]) + err(k[\Lambda_2])] \neq err(k[(\Lambda_1 + \Lambda_2)/2])$, $\forall \Lambda_1 \neq \Lambda_2$. In fact, the strategy $\frac{1}{2}[err(k[\Lambda_1]) + err(k[\Lambda_2])]$, where Λ_1 and Λ_2 correspond to sufficiently high and low Λ values, was suggested in [23] as an affordable way to optimize the k_{num} accuracy by exploring error cancellation. Although not shown here, we have confirmed the success of this strategy using the suggested solution [23]: $\Lambda_1 = 1$ and $\Lambda_2 = 1/16$.

The information offered by Figs. 2(c) and (d) also allows one to infer which Λ values select to minimize the permeability error. Their intervals are summarized in Table 3. In general, the optimum Λ interval is shifted towards larger values for finer meshes. The tuning of Λ comes out as a much more reasonable strategy to mitigate the bounce-back shortcomings than the viscosity calibration procedures [33,34], since viscosity also affects the convergence rate towards the steady state [2,23]. The possibility of differently adjusting ν and Λ is even more critical in the convergence of the Brinkman case, where keeping the number of time steps independent of flow regime the following rule-of-thumb should be satisfied with $\nu \sim k$ [12].

4.2. Porous flow

The porous flow of permeability k (and for simplicity $\nu_{\text{B}} = \nu$) introduces an additional complexity: *the Brinkman forcing*. To determine its relative importance in the solution, we define the following non-dimensional group $\sigma^2 = R^2/k$. Here, three dynamical regimes can be distinguished: (1) $\sigma \ll 1$, open Stokes flow, (2) $\sigma \sim O(1)$, intermediate Brinkman flow, and (3) $\sigma \gg 1$, very impermeable Darcy flow. When $\sigma \ll 1$, the governing equations reduce to a Stokes flow, a case already addressed in Section 4.1. Therefore, our discussion will be focused on the new features arising in the two other regimes. For the reference permeability solutions k_{th}, we take the cell model and lubrication theory solutions recently derived in [21].

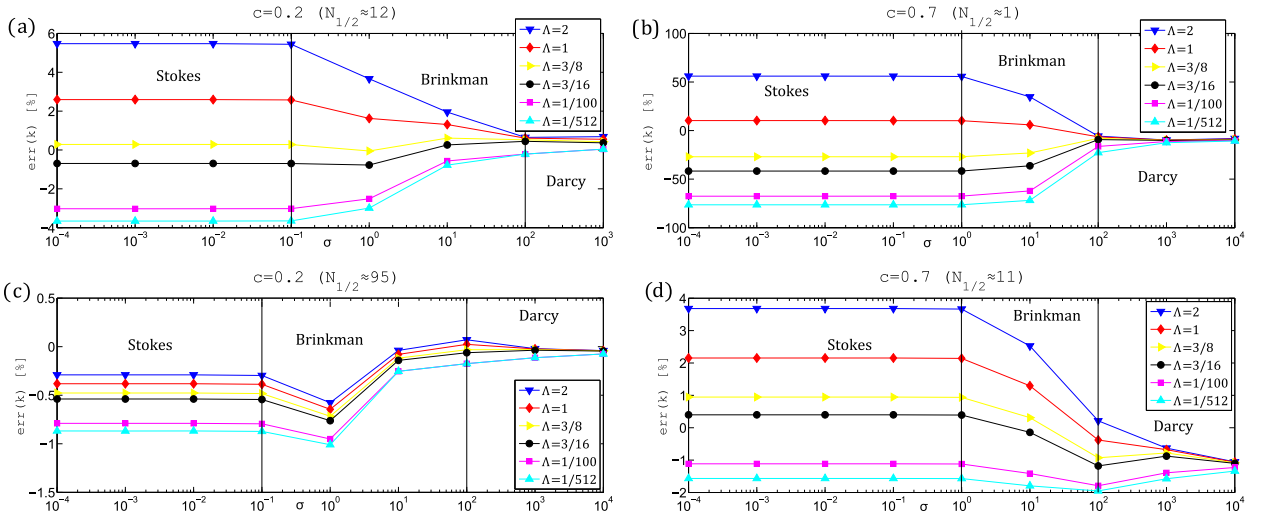

Fig. 3. (Color online.) Porous flow around solid cylinder. TRT–BF results for $err[k]$ as function of $\sigma = R/\sqrt{k}$ for different grid resolutions. Panels (a) and (c) $c = 0.2$, and (b) and (d) $c = 0.7$.

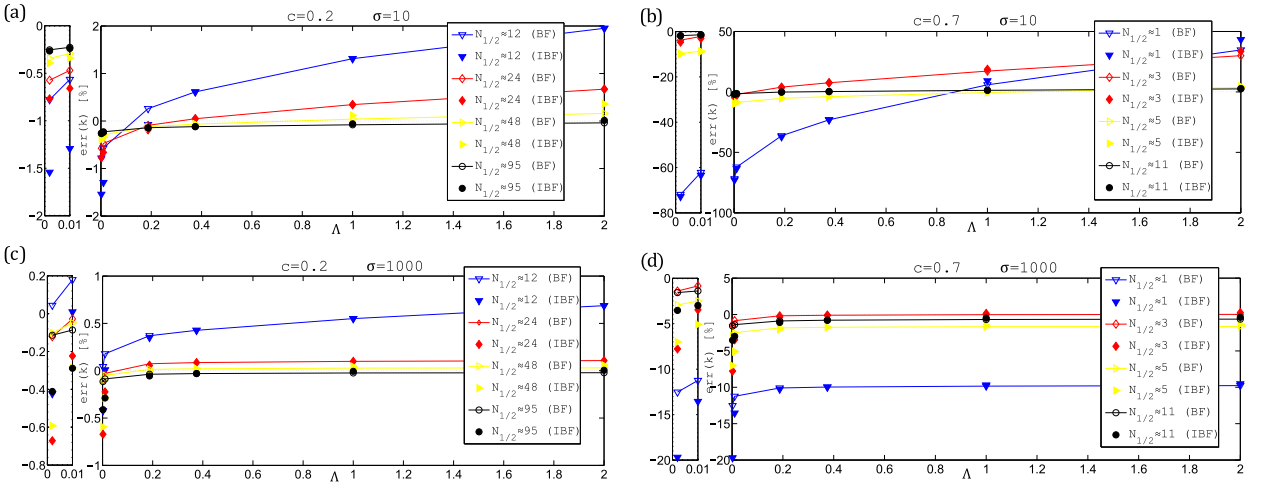

Fig. 4. (Color online.) Porous flow around solid cylinder. BF/IBF results for $err[k]$ as function of Λ for $c = 0.2$ (left) and $c = 0.7$ (right). Panels (a) and (b) Brinkman, and (c) and (d) Darcy's regime. Left sub-panels zoom in the interval $\Lambda \in [\frac{1}{152}, \frac{1}{100}]$.

Fig. 3 reveals that the error magnitude consistently decreases by increasing σ, i.e. $|err(k)|$ is maximum in Stokes' regime and it decreases towards a minimum in Darcy's one. This trend goes along with a known theoretical result [1,4], which states that the effective distance at which each solid obstacle perturbs the porous flow is also a decreasing function of σ.

Furthermore, the particular flow regime, quantified by σ, is found to have a key role on the impact of Λ over the permeability accuracy. While in Stokes flow regime the relationship between $err(k)$ and Λ is almost linear, as discussed in Section 4.1, it becomes increasingly non-linear with σ. In the limit $\sigma \gg 1$, i.e. inside Darcy's regime, $err(k)$ is almost independent of Λ, except in a narrow region of low Λ where $\frac{\partial err(k)}{\partial \Lambda}|_{(N,\sigma)} < 0$, see Fig. 4, panels (c) and (d). The impact of Brinkman's correction through coefficient δ, Eq. (8), reduces with grid resolution. Consequently, the linearity between $err(k)$ and Λ gets progressively recovered for finer grids, as attested to by the plots (c) and (d) in Fig. 4. Similar results were observed for porous flow in multi-layered and two-dimensional random media in [12].

Table 4 displays the interval of optimal Λ yielding $err(k) = 0$, as function of parameters: (i) flow regime, σ, (ii) volume fraction, c, and (iii) grid resolution in half-gap, $N_{1/2}$. In general, the optimal Λ value increases for finer grids, whereas it decreases for less permeable media (cf. results for $c = 0.2$ with $\sigma = 10$ and $\sigma = 10^3$). This behavior complies with results in porous bounded channels (e.g., Fig. 23 in [12]).

The impact of the IBF becomes more significant when the non-linear dependency on Λ is more marked. That should be expected as IBF = BF when $\sigma = 0$. In practice, the IBF forces a sharper decrease in $err(k)$ with Λ, falling into a more regular interval of Λ values, for the same error amplitude – see Fig. 4 and Table 4, especially the case when $\sigma = 10^3$ and $c = 0.2$. Such kind of behavior was also reported in [12] for porous flow in multi-layered and two-dimensional random media. In

Table 4
Porous flow around solid cylinder. Interval of optimal Λ where $err(k) = 0$ for two flow regimes: $\sigma = 10$ (Brinkman) and $\sigma = 10^3$ (Darcy), range of analysis $\Lambda \in [\frac{1}{512}, 2]$. Comparisons between BF and IBF for four resolutions at $c = 0.2$ and $c = 0.7$.

$\sigma = 10$					
$c = 0.2$	$N_{1/2}$	12	24	48	95
	BF: Λ	$[\frac{1}{100}, \frac{3}{16}]$	$[\frac{3}{16}, \frac{3}{8}]$	$[\frac{3}{8}, 1]$	> 2
	IBF: Λ	$[\frac{3}{16}, \frac{3}{8}]$	$[\frac{3}{16}, \frac{3}{8}]$	$[\frac{3}{8}, 1]$	$[1, 2]$
$c = 0.7$	$N_{1/2}$	1	3	5	11
	BF: Λ	$[\frac{3}{8}, 1]$	$[\frac{1}{100}, \frac{3}{16}]$	$[1, 2]$	$[\frac{3}{16}, \frac{3}{8}]$
	IBF: Λ	$[\frac{3}{8}, 1]$	$[\frac{1}{100}, \frac{3}{16}]$	$[1, 2]$	$[\frac{3}{16}, \frac{3}{8}]$

$\sigma = 10^3$					
$c = 0.2$	$N_{1/2}$	12	24	48	95
	BF: Λ	$]0, \frac{1}{512}]$	$[\frac{1}{100}, \frac{3}{16}]$	$[\frac{1}{100}, \frac{3}{16}]$	> 2
	IBF: Λ	$[\frac{1}{512}, \frac{1}{100}]$	$[\frac{1}{100}, \frac{3}{16}]$	$[\frac{3}{16}, \frac{3}{8}]$	$[1, 2]$
$c = 0.7$	$N_{1/2}$	1	3	5	11
	BF: Λ	> 2	$[1, 2]$	> 2	> 2
	IBF: Λ	> 2	$[\frac{3}{8}, 1]$	> 2	> 2

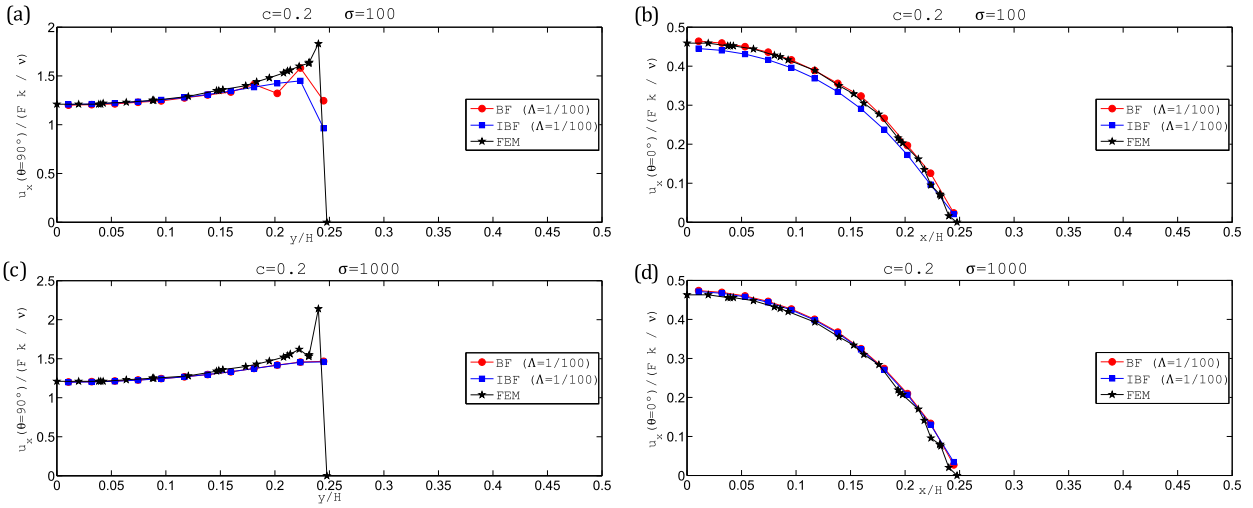

Fig. 5. (Color online.) Porous flow around solid cylinder. Half velocity profiles in vertical ((a) and (c)) and horizontal ((b) and (d)) planes, at $c = 0.2$ from BF, IBF and FEM with $N_{1/2} = 12$; $\sigma = 10^2$, Brinkman's regime, and $\sigma = 10^3$, Darcy's regime.

fact, this advantage of IBF in multi-layers is noticeable, as the accuracy level of the analytical reference solutions can be reached within a reasonable Λ interval [12].

Fig. 5 illustrates the transversal and longitudinal velocity profiles for the BF, IBF and FEM in Brinkman's and Darcy's regions. While longitudinal profiles follow a monotonic behavior, in line with the Stokes flow, the transversal velocity increases from zero, at the cylinder, to a maximum, at a small distance from the wall, and then decreases to the "unperturbed" flow value far away from the cylinder. The region adjacent to the surface of the cylinder, where the tangential velocity increases from zero at the wall to a peak value, is called the viscous sublayer, and its thickness decreases with σ^{-1} [1,4]. Hence, resolving this boundary-layer region is a challenging task for the less permeable media.

Although we can infer from Figs. 4(a) and (c) that, for the volume fraction $c = 0.2$ resolved with $N_{1/2} = 12$, the choice $\Lambda = 1/100$ is not optimal, we keep these parameters for illustrative purposes. In BF, the selection of a small Λ gives rise to negative effective viscosity and then spurious oscillations in the velocity solution. We observe this artefact in the transversal velocity profile close to the boundary region. However, these oscillations are limited to the Brinkman regime, being damped with σ until totally suppressed in Darcy's regime. Such behavior complies with BF solutions for porous bounded channels in [12], and is explained by the way the bulk solution is accommodated by the bounce-back boundary. As suggested in [12], a simple remedy to weaken these oscillations consists in locally decreasing Λ on boundary nodes, while keeping "standard" Λ values in the bulk. We have confirmed the application of this strategy to this problem. Nevertheless, a more general procedure to smoothing these spurious oscillations is delivered by the IBF scheme, see Fig. 5(a).

A confirmation that the boundary condition dictates the quality of the velocity solutions can be appreciated from a different perspective by comparisons with the FEM solutions. On the one hand, the LBM bulk solution with a very small $\Lambda = \frac{1}{100}$ features a much larger amplitude of $v < 0$ than FEM. On the other hand, while in the LBM the bounce-back boundary accommodates the wall condition implicitly, not guaranteeing exact no-slip, the FEM enforces this condition to be exact on the nodes. It is this zero velocity requirement on the boundary node that triggers the overshoot in the velocity solution. Only subsequently, and because the effective viscosity in the bulk solution is not capable of damping this perturbation, the system will react by creating wiggles. This also explains why, in general, FEM oscillations are orders of magnitude larger than LBM in bounded configurations. Such a result, illustrated in Fig. 5, agrees with solutions in porous bounded channels, see Figs. 18 and 20 in [12].

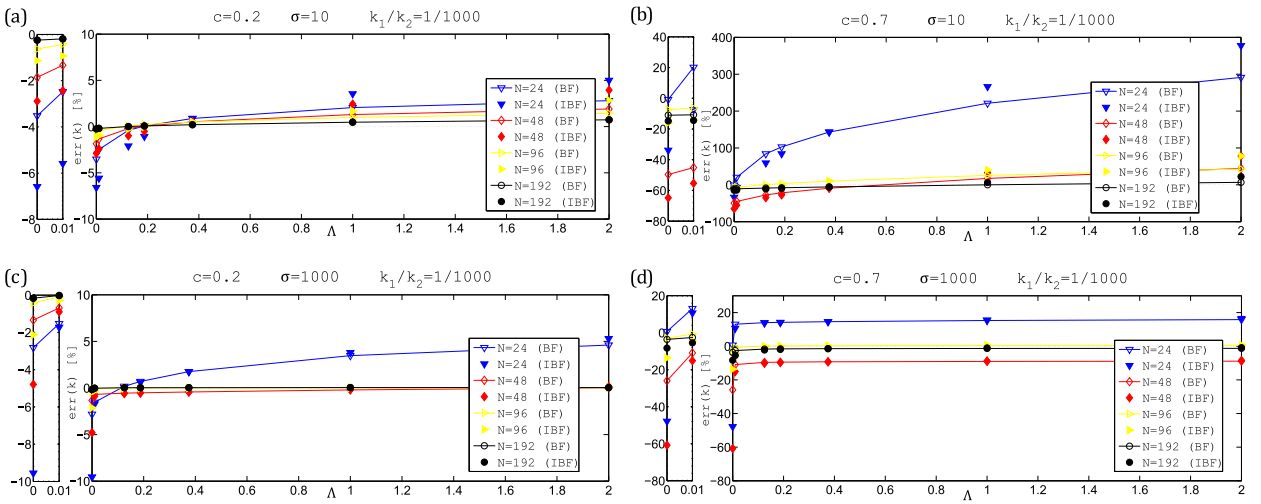

Fig. 6. (Color online.) Bimodal porous flow with $k_1 < k_2$. BF/IBF results for $err[k]$ as function of Λ for $c = 0.2$ (left) and $c = 0.7$ (right). Panels (a) and (b) $\sigma = 10$, and (c) and (d) $\sigma = 10^3$. Left sub-panels zoom in the interval $\Lambda \in [\frac{1}{10^6}, \frac{1}{100}]$.

5. Permeable inclusion: interface analysis

The bimodal configuration is characterized by the permeabilities of the matrix and of the inclusion, see Fig. 1 (where again, for simplicity, we consider $\nu_B = \nu$ in both layers). The dynamics of the system are therefore controlled by two non-dimensional groups. To enable a correspondence with the parameterization employed in the previous case, Section 4.2, we choose them as the ratio k_1/k_2 and σ defined as: (1) $\sigma^2 = R^2/k_{/\!/}$ for $k_1/k_2 < 1$, where $k_{/\!/} = c\,k_1 + (1-c)k_2$; and (2) $\sigma = R^2/k_\perp$ for $k_1/k_2 > 1$, where $k_\perp = k_1k_2/(c\,k_2 + (1-c)k_1)$. These two configurations $k_1/k_2 < 1$ and $k_1/k_2 > 1$ are indistinguishable in channels; thereby the choice for $k_{/\!/}$ and $k_\perp$ explores the similarity with parallel/perpendicular layers, where these solutions are exact in Darcy's flow. For concreteness, we restrict this analysis to permeability ratios of order 10^3, a sufficiently wide-ranging value to extract general conclusions. As references solutions for k_{th}, we take the cell model and lubrication theory solutions recently derived in [21].

5.1. Bimodal porous flow: $k_1 < k_2$

Since the inclusion is 10^3 times less permeable than the outside porous medium, the present configuration resembles the case of porous flow around a solid obstacle, discussed in Section 4.2. The difference is that the effective permeability is controlled by the interface condition. Notice that "partial bounce-back schemes" (also known as gray LBM [15]) model the impermeable geometry by assigning a small permeability ratio. Hence, this study also provides insight on the capabilities of such schemes.

Comparing Fig. 6 with Fig. 4, we notice that, qualitatively, the two cases have comparable trends: the magnitude of $err(k)$ increases with σ and the non-linear relationship between $err(k)$ and Λ also increases with σ. Quantitatively, there are however more significant differences. In coarse resolutions, the interface condition gives rise to $err(k)$, an order of magnitude larger compared to bounce-back. This suggests that the interface condition is considerably less accurate in the description of permeable structures than in that of solid ones. A similar conclusion was found in channels (see Fig. 10 in [12]).

Table 5 displays the interval of optimal Λ that sets $err(k) = 0$, as a function of the following parameters: (1) flow regime, σ, (2) volume fraction, c, and (3) domain resolution, N. Unlike in the previous cases, in this problem solutions appear more scattered. Still, the generic trend that the IBF possesses larger optimal Λ values, compared to the BF, is regularly observed. This result is in agreement with the porous multi-layered and random configurations studied in [12].

Fig. 7 displays transversal and longitudinal velocity profiles for the BF, IBF and FEM at $\sigma = 10$. We focus on this regime since it is where, according to the permeability analysis, larger errors occur. For $c = 0.2$, the velocity profiles display qualitative similarities with the case of a porous flow around solid inclusions. Nevertheless, here boundary layers appear wider because the velocity transition from matrix to inclusion is smoother. This behavior is explained by the different way velocity profiles are accommodated by bounce-back and interface conditions. The effect of decreasing Λ is twofold: it reduces the interface velocity jump, but it amplifies the oscillations in the velocity field (both in vertical and horizontal directions). Hence, the adoption of the IBF scheme becomes recommendable, as it virtually suppresses oscillations (although not extinguishing them to round-off precision as in channels). At $c = 0.7$, as the outside region is resolved by few nodes, there is a larger jump in the velocity continuity across the interface. The interface accuracy is strongly affected by Λ and whether the BF or IBF is used, see Fig. 7, panels (c) and (d). The FEM velocity profiles display, in general, larger spurious oscillations,

Table 5
Bimodal porous flow with $k_1 < k_2$. Interval of optimal Λ where $err(k) = 0$ for two flow regimes: $\sigma = 10$ and $\sigma = 10^3$, range of analysis $\Lambda \in [\frac{1}{10^6}, 2]$. Comparisons between BF and IBF for four resolutions at $c = 0.2$ and $c = 0.7$.

$\sigma = 10$					
$c = 0.2$	N	24	48	96	192
	BF: Λ	$[\frac{1}{8}, \frac{3}{16}]$	$[\frac{1}{8}, \frac{3}{16}]$	$[\frac{1}{100}, \frac{1}{8}]$	$[\frac{1}{100}, \frac{1}{8}]$
	IBF: Λ	$[\frac{3}{16}, \frac{3}{8}]$	$[\frac{3}{16}, \frac{3}{8}]$	$[\frac{3}{16}, \frac{3}{8}]$	$[\frac{1}{100}, \frac{1}{8}]$
$c = 0.7$	N	24	48	96	192
	BF: Λ	$[\frac{1}{10^6}, \frac{1}{100}]$	$[\frac{3}{8}, 1]$	$[\frac{1}{100}, \frac{1}{8}]$	$[1, 2]$
	IBF: Λ	$[\frac{1}{100}, \frac{1}{8}]$	$[\frac{3}{8}, 1]$	$[\frac{3}{16}, \frac{3}{8}]$	$[\frac{3}{8}, 1]$

$\sigma = 1000$					
$c = 0.2$	N	24	48	96	192
	BF: Λ	$[\frac{1}{100}, \frac{1}{8}]$	$[1, 2]$	$[\frac{3}{16}, \frac{3}{8}]$	$[\frac{1}{100}, \frac{1}{8}]$
	IBF: Λ	$[\frac{1}{100}, \frac{1}{8}]$	$[1, 2]$	$[\frac{3}{16}, \frac{3}{8}]$	$[\frac{1}{100}, \frac{1}{8}]$
$c = 0.7$	N	24	48	96	192
	BF: Λ	$]0, \frac{1}{10^6}]$	> 2	$[\frac{1}{100}, \frac{1}{8}]$	> 2
	IBF: Λ	$[\frac{1}{10^6}, \frac{1}{100}]$	> 2	$[\frac{3}{16}, \frac{3}{8}]$	> 2

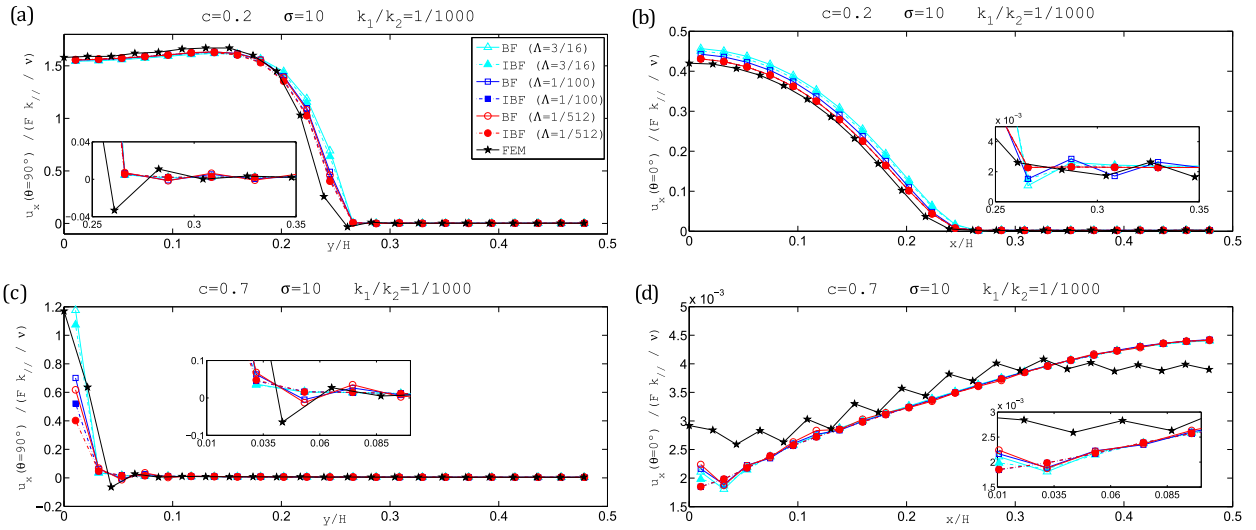

Fig. 7. (Color online.) Bimodal porous flow with $k_1 < k_2$. Half profiles of velocity in vertical ((a) and (c)) and horizontal ((b) and (d)) planes, from BF, IBF and FEM resolved with $N = 48$; $c = 0.2$ in (a) and (b) and $c = 0.7$ in (c) and (d). Insets zoom in the velocity inside the less permeable layer.

although we note that, in principle, the apparent viscosity in FEM is not as negative as in LBM. This provides a supplemental confirmation that the reason for this artefact does not come from the bulk alone, but rather from the enforcement of velocity and stress continuity conditions at grid nodes, which does not guarantee the necessary freedom for the smooth accommodation of the sharp velocity gradient across the interface, more flexible to achieve with the LBM implicit interface condition. As this result was also observed in channels, further confirmation is given of the fact that this problem is not due to the staircase discretization.

5.2. *Bimodal porous flow: $k_1 > k_2$*

This case studies the inverse configuration of Section 5.1. Since the inclusion is 10^3 times more permeable than the outside medium, this system is illustrative of porous flow across open fractures. In fact, although seldom considered in LB studies, this configuration is a rather challenging problem for numerical simulations as patent in the $err(k)$ magnitude in Fig. 8. Similarly to previous cases, the relationship between $err(k)$ and Λ experiences a growing non-linear dependency with the flow regime σ. At large σ, the permeability solution holds nearly unchanged, while decreasing abruptly at very small Λ. This non-linear dependency on Λ tends to decrease towards a more linear one as the mesh is refined. As expected, the IBF solution only displays quantitative differences when the Λ-dependency of the BF solution is significant. In all cases tested herein, the LBM permeability is always overestimated. Consequently, there is no optimal Λ where the reference solution can be reached.

To illustrate the difficulties experienced by the LBM in this problem, let us focus on the most challenging regime: $\sigma = 1000$. Fig. 9 depicts vertical and horizontal velocity profiles for both low and high volume fractions. Once again, the critical feature dictating the accuracy of the solution is the interface condition. In FEM, the velocity and stress continuity conditions are enforced in nodes, and this leads to severe oscillations in the open layer (inside the inclusion). We note the FEM profile, although affected by oscillations, is more likely to average around the correct velocity magnitude, since its discrete interface condition operates with the same rules of bulk nodes, hence free from jumps in the solutions. On the other hand, the relief of such an explicit interface condition produces large interface jumps, as displayed in LBM results.

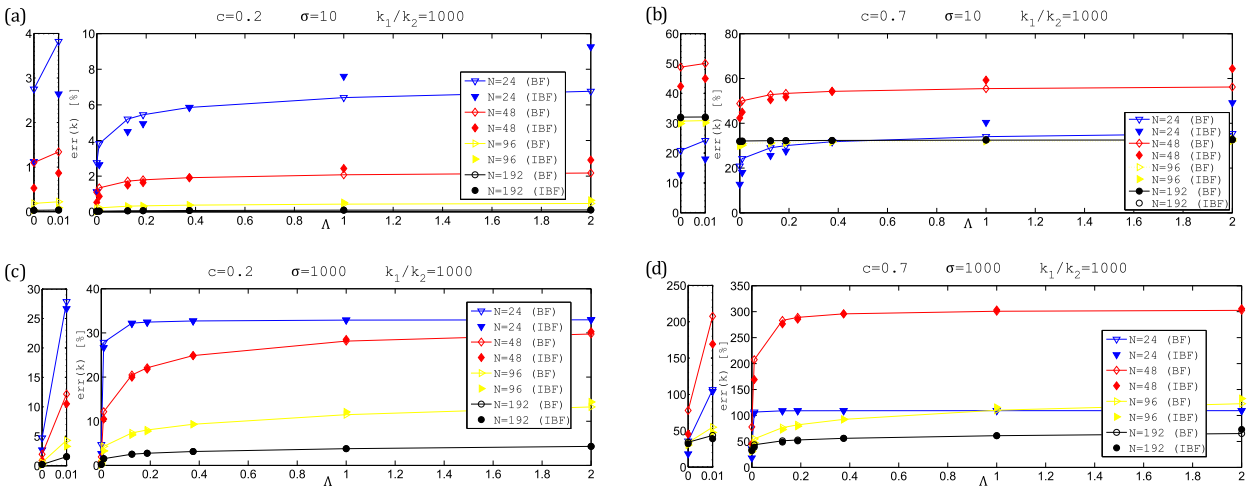

Fig. 8. (Color online.) Bimodal porous flow with $k_1 > k_2$. BF/IBF results for $err[k]$ as function of Λ for $c = 0.2$ (left) and $c = 0.7$ (right). Panels (a) and (b) $\sigma = 10$, and (c) and (d) $\sigma = 10^3$. Left sub-panels zoom in the interval $\Lambda \in [\frac{1}{10^6}, \frac{1}{100}]$.

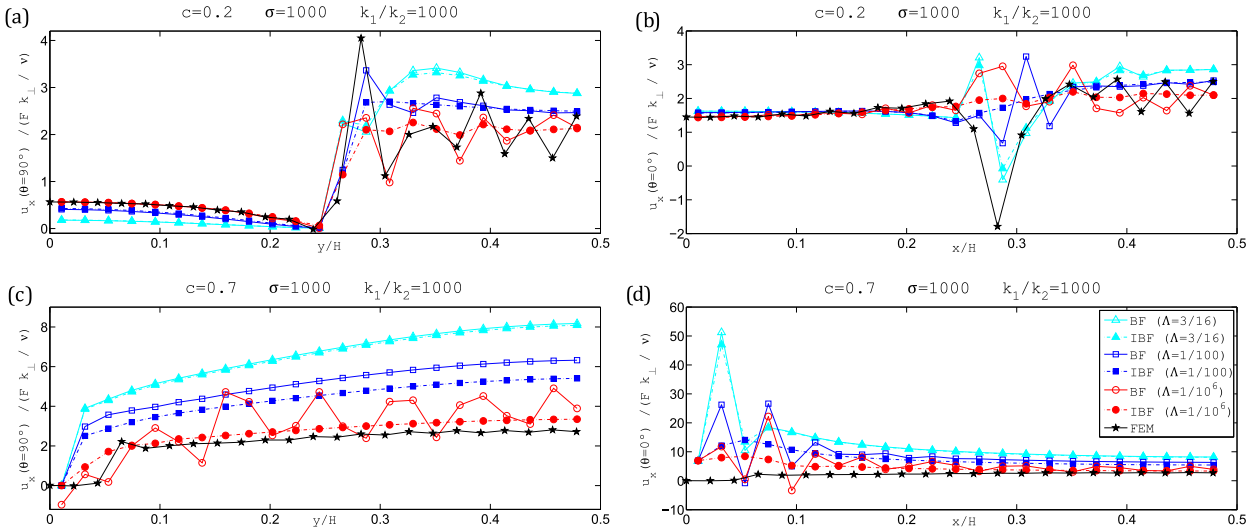

Fig. 9. (Color online.) Bimodal porous flow with $k_1 > k_2$. Half profiles of velocity in vertical ((a) and (c)) and horizontal ((b) and (d)) planes, from BF, IBF and FEM resolved with $N = 48$; $c = 0.2$ in (a) and (b) and $c = 0.7$ in (c) and (d).

However, this defect can be mitigated by decreasing Λ, yet at the cost of amplifying spurious oscillations. Again, a remedy to damp these wiggles relies on the use of the IBF.

Indeed, the superiority of the IBF over BF is even more notorious at $c = 0.7$. Owing to the poorly resolved outside impermeable layer and the large permeability contrast across the interface, the interface condition gives rise to a significant velocity jump, which in turn causes a large overestimation of the velocity inside the open inclusion, see Fig. 9, (c) and (d). The reduction of Λ brings the LBM velocity profile close to the FEM one. Since the use of small Λ values introduces, in this case, unacceptable oscillations, the use of IBF becomes imperative to suppress them (at least partially). Everything considered, IBF with small Λ generates velocity profiles more in agreement with the FEM solution, while generally less oscillatory than FEM – see Fig. 9.

6. Conclusion

For benchmarking the TRT–LBM and FEM Brinkman schemes, the present work proposed the simulation of porous flow across a periodic square array of solid or permeable cylindrical inclusions, exploring recently derived permeability predictions [21]. This numerical study pursued two main objectives. First, to understand how the bulk, boundary and interface analyses, developed for heterogeneous channels in [12], apply on more complex geometries. Second, to assess whether the scheme developed in [12] to vanish oscillations in heterogeneous channels, called IBF (i.e. improved Brinkman-forcing model), also holds in this non-trivial configuration. In order to address these two questions, we have considered four

principal flow configurations, and evaluated the performance of the numerical schemes based on (1) the accuracy of permeability predictions, and (2) the quality of velocity fields.

The first case was the Stokes flow around a solid cylinder. The purpose of this "warm-up" test was assessing the ability of the bounce-back rule, which is typically used in the context of porous media flows, to describe a flow around a curved surface. At coarse resolutions, we confirmed that the permeability error is clearly dominated by the Λ-dependent shift of no-slip location, where Λ is the additional degree of collision of the TRT model. Here, both large and small Λ values produce very inaccurate solutions, which converge towards zero for finer meshes. For a fixed grid, the $err(k)$ varies almost linearly with Λ, with its slope decreasing with grid resolution. As for the optimal Λ in Stokes' regime, according to [23], the typical rule-of-thumb is $\Lambda \in [\frac{1}{8}, \frac{3}{8}]$, which fits reasonably well in our coarsest grid solutions. The general trend is: the finer the mesh is, the larger the optimum Λ where $err(k) = 0$ is. We note that, although the minimization of $err(k)$ is also possible with the BGK operator through ν-calibration [33,34], yet this procedure is computationally inefficient as ν also controls the steady-state convergence rate [2,23].

The second test involved a porous (Brinkman) flow around a solid cylinder. This problem covers three flow regimes: Stokes, Brinkman and Darcy, by decreasing order of assigned permeability. We observed that the accuracy of the numerical solutions consistently improves from Stokes' regime to Darcy's one. At the same time, the less-permeable the surrounding porous matrix is, the more non-linear the dependency of $err(k)$ on Λ becomes. This is explained by bulk and boundary discretizations being affected by Λ through a Brinkman forcing correction, which is also weighted by a flow-dependent parameter, recall Section 3. Generally, the optimal Λ value increases with mesh resolution, whereas it decreases for less permeable media. Concerning the quality of velocity fields, spurious oscillations do not develop monotonically with the media's permeability, in agreement with bounded heterogeneous channels [12]. When BF displays velocity wiggles, IBF was confirmed as a competent strategy to suppress them. Comparatively, FEM displays velocity oscillations of larger amplitude, which increase monotonically when the medium's permeability decreases.

The third test concerned a porous flow across a permeable cylinder, though less permeable than the outside flow. This problem is controlled by the interface condition. While the $err(k)$ dependency on either Λ or the flow regime displayed the same general trends of the solid case, a larger error magnitude was observed here, which hints to the inferior precision of the interface condition. Also, the fact that the intervals of optimal Λ exhibited a rather more irregular behavior, compared to reference solutions in channels [12], evidenced the non-negligible role of the geometrical discretization error in this case. To improve this deficiency, explicit higher-order boundary and/or interface methods for LBM shall be developed, taking into account the Brinkman forcing. Such a task will be pursued in future studies.

The fourth test was also porous flow across a permeable cylinder, but with the inclusion more permeable than the outside medium. This was possibly the most challenging configuration, among all cases studied, as attested to by the large magnitude of $err(k)$. Here, LBM velocity solutions were consistently over-predicted, due to large velocity jumps across the interface. This defect increased for coarser meshes and/or for smaller permeability systems. Although the velocity jump can be reduced by decreasing Λ, this procedure wildly amplified numerical oscillations. Thereby, the use of the IBF is critical in this case. Indeed, the IBF has diverse advantages, namely: (1) it retains the linearity of the modeled Brinkman equation with viscosity, like the BF and unlike "partial-bounce-back" schemes, and (2) it operates locally, either in 2D or 3D, by simply self-adjusting its viscosity eigenvalue according to the local permeability properties. In FEM the velocity is also oscillatory. Yet, due to the absence of interface jumps, its value averages around a reasonable solution, making the presence of wiggles overlooked in permeability measurements. As future work, and since these non-physical velocity oscillations are general features affecting under-resolved simulations (where transport problems in porous media typically operate), it would be interesting to quantify their impact on the solution to associated convection–diffusion problems.

References

[1] A. Bejan, I. Dincer, S. Lorente, A.F. Miguel, A.H. Reis, Porous and Complex Flow Structures in Modern Technologies, Springer, New York, 2004.
[2] L. Talon, D. Bauer, N. Gland, S. Youssef, H. Auradou, I. Ginzburg, Assessment of the two relaxation time lattice-Boltzmann scheme to simulate Stokes flow in porous media, Water Resour. Res. 48 (2012) W04526.
[3] H.C. Brinkman, A calculation of the viscous force exerted by a flowing fluid on a dense swarm of particles, Appl. Sci. Res. 1 (1947) 27–34.
[4] K. Vafai, Handbook of Porous Media, Taylor & Francis, New York, 2005.
[5] C.K. Aidun, J.R. Clausen, Lattice-Boltzmann method for complex flows, Annu. Rev. Fluid Mech. 42 (2010) 439–472.
[6] M.A. Spaid, F. Phelan, Lattice Boltzmann methods for modeling microscale flow in fibrous porous media, Phys. Fluids 9 (1997) 2468.
[7] D.M. Freed, Lattice-Boltzmann method for macroscopic porous media modeling, Int. J. Mod. Phys. C 9 (1998) 1491–1503.
[8] Z. Guo, C. Zhao, Lattice Boltzmann model for incompressible flows through porous media, Phys. Rev. E 66 (2002) 036304.
[9] Q. Kang, D. Zhang, S. Chen, Unified lattice Boltzmann method for flow in multiscale porous media, Phys. Rev. E 66 (2002) 056307.
[10] T. Seta, Lattice Boltzmann method for fluid flows in anisotropic porous media with Brinkman equation, J. Therm. Sci. Technol. 4 (2009) 116–127.
[11] I. Ginzburg, Comment on "an improved gray lattice Boltzmann model for simulating fluid flow in multi-scale porous media": intrinsic links between LBE Brinkman schemes, Adv. Water Resour. (2015), http://dx.doi.org/10.1016/j.advwatres.2014.05.007, in press.
[12] I. Ginzburg, G. Silva, L. Talon, Analysis and improvement of Brinkman lattice Boltzmann schemes: bulk, boundary, interface. Similarity and distinctness with finite-elements in heterogeneous porous media, Phys. Rev. E 91 (2015) 023307.
[13] Y. Gao, M.M. Sharma, A LGA model for fluid flow in heterogeneous porous media, Transp. Porous Media 17 (1994) 1–17.
[14] S.D.C. Walsh, H. Burwinkle, M.O. Saar, A new partial bounce back lattice Boltzmann method for fluid flow through heterogeneous media, Comput. Geosci. 36 (2009) 1186–1193.
[15] J. Zhu, J. Ma, An improved gray lattice Boltzmann model for simulating fluid flow in multi-scale porous media, Adv. Water Resour. 56 (2013) 61–76.
[16] H. Yoshida, H. Hayashi, Transmission–reflection coefficient in the lattice Boltzmann method, J. Stat. Phys. 155 (2014) 277–299.

[17] R. Li, Y.S. Yang, J. Pan, G.G. Pereira, J.A. Taylor, B. Clennel, C. Zou, Lattice Boltzmann modeling of permeability in porous materials with partially percolating voxels, Phys. Rev. E 90 (2014) 033301.
[18] I. Ginzburg, Consistent lattice Boltzmann schemes for the Brinkman model of porous flow and infinite Chapman–Enskog expansion, Phys. Rev. E 77 (2008) 066704.
[19] Y. Qian, D. d'Humières, P. Lallemand, Lattice BGK models for Navier–Stokes equation, Europhys. Lett. 17 (1992) 479–484.
[20] I. Ginzburg, Lattice Boltzmann modeling with discontinuous collision components: hydrodynamic and advection–diffusion equations, J. Stat. Phys. 126 (2007) 157–206.
[21] G. Silva, I. Ginzburg, Stokes–Brinkman–Darcy solutions of bimodal porous flow across periodic array of permeable cylindrical inclusions: cell model, lubrication theory and LBM/FEM numerical simulations, submitted for publication.
[22] I. Ginzburg, P.M. Adler, Boundary flow condition analysis for the three-dimensional lattice Boltzmann model, J. Phys. II 4 (1994) 191–214.
[23] S. Kirevich, I. Ginzburg, U. Tallarek, Coarse- and fine-grid numerical behavior of MRT/TRT lattice Boltzmann schemes in regular and random sphere packings, J. Comp. Physiol. 281 (2014) 708–742.
[24] A.S. Sangani, A. Acrivos, Slow flow past periodic arrays of cylinders with application to heat transfer, Int. J. Multiph. Flow 8 (1982) 193–206.
[25] J. Happle, Viscous flow relative to arrays of cylinders, AIChE J. 5 (1959) 174–177.
[26] S. Kuwabara, The forces experienced by randomly distributed parallel circular cylinders or spheres in a viscous flow at small Reynolds numbers, J. Phys. Soc. Jpn. 14 (1959) 527–532.
[27] J.B. Keller, Viscous flow through a grating or lattice of cylinders, J. Fluid Mech. 18 (1964) 94–96.
[28] F.R. Phelan, G. Wise, Analysis of transverse flow in aligned fibrous porous media, Composites 27A (1995) 25.
[29] J.N. Reedy, An Introduction to the Finite Element Method, 2nd edition, McGraw–Hill International Editions, 1993.
[30] COMSOL, Multiphysics, Reference guide, 2012.
[31] S. Bogner, S. Mohanty, U. Rude, Drag correlation for dilute and moderately dense fluid-particle systems using the lattice Boltzmann method, Int. J. Multiph. Flow 68 (2014) 71–79.
[32] R.W. Nash, H.B. Carver, M.O. Bernabeu, J. Hetherington, D. Groen, T. Krüger, P.V. Coveney, Choice of boundary condition for lattice-Boltzmann simulation of moderate Reynolds number flow in complex domains, Phys. Rev. E 89 (2014) 023303.
[33] A.J.C. Ladd, Numerical simulations of particulate suspensions via a discretized Boltzmann equation. Part 1. Theoretical foundation, J. Fluid Mech. 271 (1994) 285–309.
[34] M.A. van der Hoef, R. Beetstra, J.A.M. Kuipers, Lattice-Boltzmann simulations of low-Reynolds-number flow past mono- and bidisperse arrays of spheres: results for the permeability and drag force, J. Fluid Mech. 528 (2005) 233–254.